Radar sounding of subsurface water-ice in eastern Coprates and Capri Chasmata, Mars

Rina Noguchi[1], Ken Ishiyama[2], Atsushi Kumamoto[3], Chihiro Uemura[4], Yasumasa Kasaba[3], Tomohiro Usui[1], Aina Oura[3], and Daigo Shoji[5]

[1]Institute of Space and Astronautical Science, Japan Aerospace Exploration Agency
[2]National Institute of Technology, Tsuruoka College
[3]Tohoku University
[4]SOKENDAI (Graduate University for Advanced Studies)
[5]Earth-Life Science Institute, Tokyo Institute of Technology

November 21, 2022

Abstract

We surveyed the subsurface structure in eastern Coprates and Capri Chasmata in the equatorial region using high-resolution visible images, digital terrain models, and radar sounding data. We identified subsurface reflectors in four areas of the chasmata. At the stratigraphic exposure on the chasmata walls, the corresponding depth of the reflector is ˜60 m. The bulk dielectric constants of the layers above the reflectors are calculated as 3.4-4.0, suggesting a rock-air mixture with ˜46.1% porosity, or a rock-air-ice mixture with ˜21.2% water-ice fraction. Recent climate models suggest that water-ice is unstable on the surface around the equatorial regions. However, considering the recent high obliquity that occurred ˜0.4 Ma and a slow diffusivity of water-ice, the existence of subsurface water-ice deeper than a few meters cannot be ruled out. If water-ice is actually contained in the layer, our results show the maximum volume of putative water-ice in the chasmata is 16.6 km.

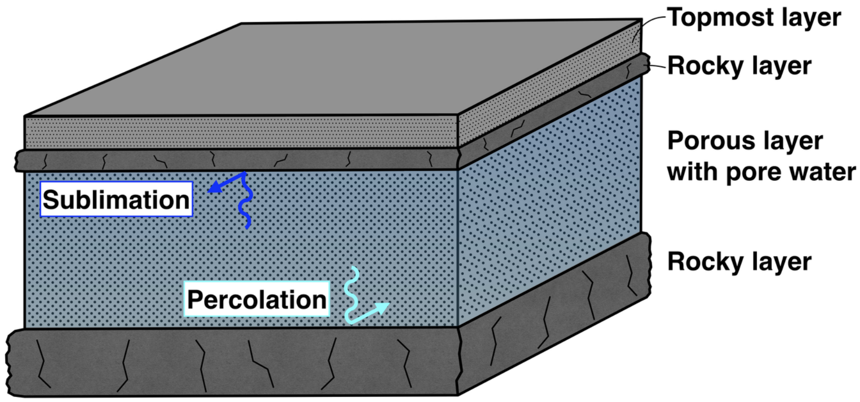

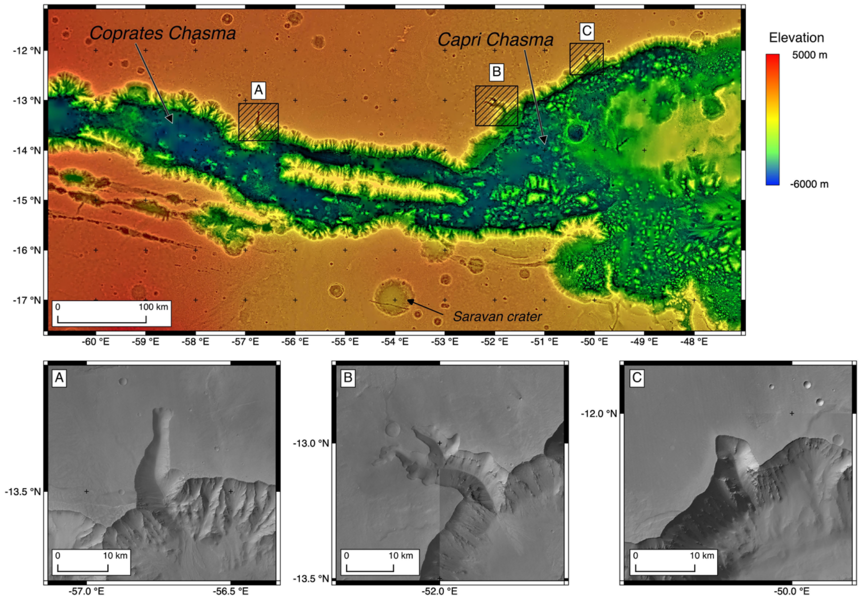

Coprates Chasma
Capri Chasma
Saravan crater
Elevation
5000 m
-6000 m
A
B
C
-12 °N
-13 °N
-14 °N
-15 °N
-16 °N
-17 °N
0
100 km
-60 °E
-59 °E
-58 °E
-57 °E
-56 °E
-55 °E
-54 °E
-53 °E
-52 °E
-51 °E
-50 °E
-49 °E
-48 °E
-13.5 °N
10 km
-57.0 °E
-56.5 °E
-13.0 °N
-13.5 °N
-52.0 °E
-12.0 °N
-50.0 °E

Radar sounding of subsurface water-ice in eastern Coprates and Capri Chasmata, Mars

R. Noguchi[1], K. Ishiyama[1,2], A. Kumamoto[3], C. Uemura[4], Y. Kasaba[3], T. Usui[1,5], A. Oura[3], and D. Shoji[5]

[1]Institute of Space and Astronautical Science, Japan Astronautical Exploration Agency, 3-1-1 Yoshinodai, 252-5210, Sagamihara, Kanagawa, Japan
[2]National Institute of Technology, Tsuruoka College, 104 Sawada, Inooka, Tsuruoka, Yamagata 997-8511, Japan
[3]Tohoku University, Aramaki-Aza-Aoba 6-3, Aoba-ku, Sendai, Miyagi, 980-8578, Japan
[4]SOKENDAI (Graduate University for Advanced Studies), 3-1-1 Yoshinodai, Sagamihara, Kanagawa, 252-5210, Japan
[5]Earth-Life Science Institute, Tokyo Institute of Technology, 2-12-1 Ookayama, Meguro, Tokyo, 152-8550, Japan

Key Points:

- We identified subsurface reflectors in four areas in the eastern Coprates and Capri Chasmata based on SHARAD data.
- Dielectric constants estimated using HiRISE data provide the upper limit of the possible volume fraction of water-ice as 21.2 %.
- This upper limit yields the maximum volume of putative subsurface water-ice in the chasmata of 16.6 km^3.

Corresponding author: Rina Noguchi, `r-noguchi@planeta.sci.isas.jaxa.jp`

Corresponding author: Tomohiro Usui, `usui.tomohiro@jaxa.jp`

Abstract

We surveyed the subsurface structure in eastern Coprates and Capri Chasmata in the equatorial region using high-resolution visible images, digital terrain models, and radar sounding data. We identified subsurface reflectors in four areas of the chasmata. At the stratigraphic exposure on the chasmata walls, the corresponding depth of the reflector is ∼60 m. The bulk dielectric constants of the layers above the reflectors are calculated as 3.4–4.0, suggesting a rock-air mixture with ∼46.1% porosity, or a rock-air-ice mixture with ¡21.2% water-ice fraction. Recent climate models suggest that water-ice is unstable on the surface around the equatorial regions. However, considering the recent high obliquity that occurred ∼0.4 Ma and a slow diffusivity of water-ice, the existence of subsurface water-ice deeper than a few meters cannot be ruled out. If water-ice is actually contained in the layer, our results show the maximum volume of putative water-ice in the chasmata is 16.6 km3.

1 Introduction

While the effect of water on the Martian climate and geological evolution is important, the distribution of subsurface water/ice is not well known. Among the remote sensing methods, the radar sounding technique has the most potential to visualize the subsurface structure of Mars. This technique has revealed subsurface icy layering (*Putzig et al.*, 2018) and possible subglacial liquid water beneath the polar caps (*Orosei et al.*, 2018). A recent encompassing and amalgamating survey with other datasets has revealed the extent of the cryosphere using radar sounding data (*Bramson et al.*, 2015; *Morgan et al.*, 2019; *Stuurman et al.*, 2017). For example, *Bramson et al.* (2015) estimated the existence of excess ice (higher water-ice abundances than the maximum porosity of dry regolith) due to low dielectric constants estimated by compiling exposed crater terraces and the subsurface radar reflectance. Thus, compiling various remote sensing data including the radar sounding technique will unveil the water-ice beneath the surface of Mars.

Interestingly, in contrast to the climate models that imply the ice is unstable, the existence of subsurface water-ice on current Mars at mid-latitudes has been indicated/suggested by several previous studies based on remote sensing observations (*Bramson et al.*, 2015; *Byrne et al.*, 2009; *Dundas et al.*, 2014; *Stuurman et al.*, 2017). From current Martian climate conditions, the existence of subsurface water-ice is not expected (e.g., *Schorghofer and Aharonson*, 2005). One piece of evidence for the existence of subsurface water-ice et the current mid-latitudes is the ice excavated by newly formed impact craters (*Byrne et al.*, 2009; *Dundas et al.*, 2014). The radar sounding technique has found possible subsurface extents of water-ice in mid-latitude planitiae (*Bramson et al.*, 2015; *Stuurman et al.*, 2017). Analyzing morphometry of expanded secondary craters, *Viola et al.* (2015) estimated that possible subsurface water-ice in Arcadia Planitia has been preserved for tens of millions of years. Thus, in the mid-latitude area, it seems that water-ice is preserved for a longer time than suggested by climate modeling evaluations.

On the other hand, at low-latitudes, current water-ice in the shallow subsurface has not been observed explicitly, although remnants of mountain glaciers have been found (*Head and Marchant*, 2003; *Milkovich et al.*, 2006). Here, to survey the subsurface structure in the equatorial region, we compile visible images, topographic data, and radar sounding data at one of the largest outcrops on Mars: Valles Marineris. Valles Marineris has been characterized by water-related geologic features such as a distribution of a variety of aqueous minerals (e.g., sulfates *Chojnacki and Hynak*, 2008) and fluvial topography (*Carr and Head*, 2010, and references therein). Furthermore, swarms of recurring slope lineae (RSLs) possibly induced by water-related recurrent surface activity have been investigated (*Chojnacki et al.*, 2016; *Stillman et* *al.*, 2017), although the formation mechanisms are still under debate (e.g., *Dundas et al.*, 2017). Thanks to those water-related features, dense and high-resolution remote sensing datasets have been developed. Subsurface radar reflectors exist in several areas of the Valles Marineris plateau (*Smith et al.*, 2019). Large and clear stratigraphy exposed on the walls could be assigned to those subsurface radar reflectors. A flat and lightly cratered surface in the plateau of eastern Coprates and Capri Chasmata, the eastern portion of Valles Marineris, provides a reliable dataset for radar sounding analysis, since rough surface topography causes artificial reflectors such as surface clutter echos (*Seu et al.*, 2004). In this context, we selected eastern Coprates and Capri Chasmata as targets of this compiling study.

2 Method

Beyer and McEwen (2005) described the stratigraphy of eastern Coprates and northern Capri Chasmata in detail using visible images, infrared images, spectrum data, and topographic data. There are exposed alternating thin strong layers and thicker sequences of relatively weak layers (*Beyer and McEwen*, 2005). The topmost strong layer is a 10 m-thick dark-toned layer and is thought to be a Hesperian basaltic lava flow (*Witbeck et al.*, 1991). The sequences of relatively weak layers have been indicated as sequences of thin flows interbedded with tephra or other sediments (*Beyer and McEwen*, 2005).

At the point of interest, we described the exposed stratigraphy of the chasma wall using visible images and topographic data (Fig.3B). Firstly, layers on outcrops that are not covered with talus deposits were identified on HiRISE images. We measured the depths and thicknesses of identified layers on high-resolution topographic data HiRISE digital terrain models (DTMs). We used two-origin HiRISE DTMs 1) produced by NASA/JPL/University of Arizona/USGS and 2) generated using MarsSI (`https://marssi.univ-lyon1.fr/MarsSI/`), which includes processes using Ames Stereo Pipeline (*Quantin-Nataf et al.*, 2018). The procedure on MarsSI is 1) import HiRISE EDR images (raw data) and calibrate, 2) create DTMs, and 3) align created DTMs to the MOLA data. Due to the availability of HiRISE DTMs, we described stratigraphy at two points: point 1 and 2 (Fig.2). Since it is difficult to describe facies in detail even in HiRISE images, we briefly classified layers into three types by their appearance: fine, coarse, and very coarse. The fine layers have no obvious boulders/rocks inside and correspond to the relatively weak layers shown in *Beyer and McEwen* (2005). The very coarse layers look like fractured lava rock or are boulder-rich. Some of them are described as the strong layers and interpreted as the last basaltic lava flow by *Beyer and McEwen* (2005). Coarse layers have an intermediate appearance between fine and very coarse layers. Based on this classification, stratigraphic columns were created using StratGen (version 1.6.0) produced by Indiana University, Indiana Geological Survey. We compared possible depths of subsurface reflectors and those stratigraphies, then considered component materials with plausible dielectric constant.

We identified subsurface reflectors on radargrams generated from radar sounding data obtained by Mars SHAllow RADar sounder (SHARAD) on Mars Reconnaissance Orbiter (MRO) (*Seu et al.*, 2004). The operating frequency of SHARAD is 15 – 25 MHz, the bandwidth of which (10 MHz) corresponds to the vertical resolution of 8.4 m assuming pure water-ice (dielectric constant = 3.15) or 5.3 m for rock with a dielectric constant = 8 (*Bramson et al.*, 2015). The spatial resolution, based on synthetic aperture processing, is 0.3 to 1 km along the track direction and 3 to 7 km along the cross-track direction (*Seu et al.*, 2004). The MRO MARS SHARAD 5 RADARGRAM V1.0 we used was provided by the SHARAD team via the Geosciences node of the Planetary Data System (PDS) at `http://pds-geosciences`

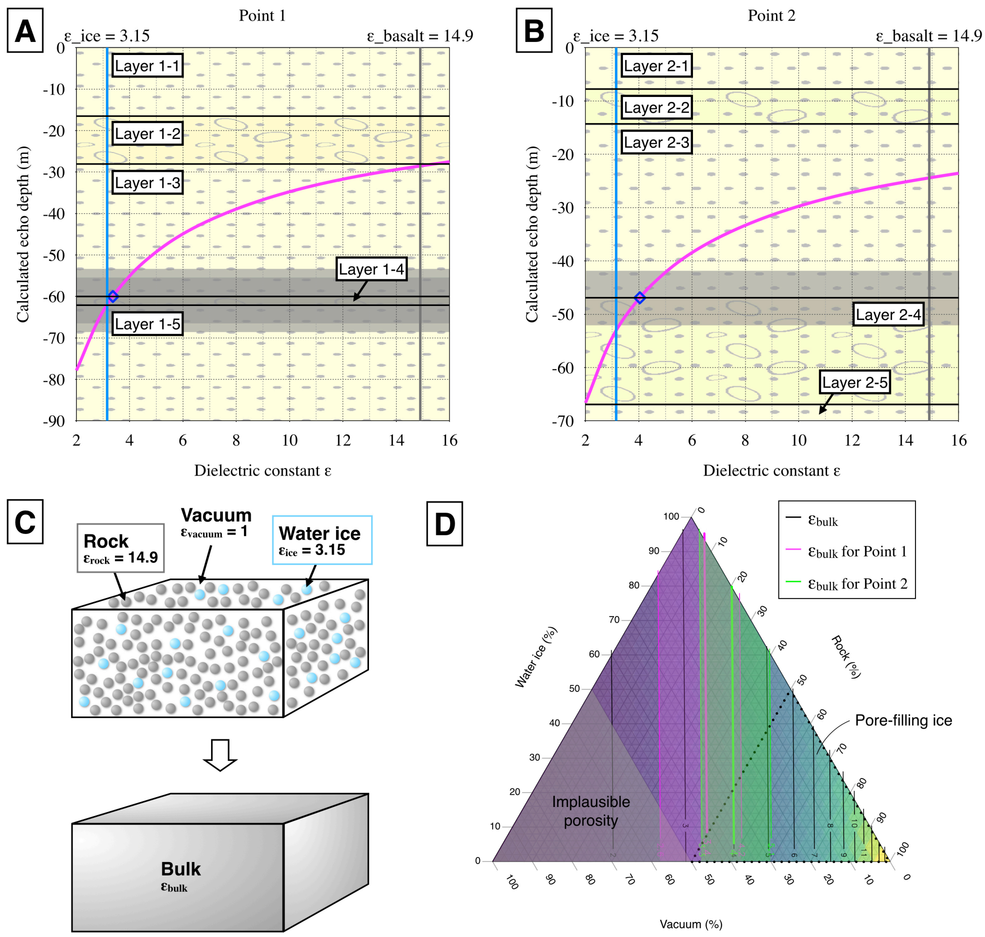

Figure 1. Estimation of dielectric constants (magenta lines) at point 1 (A) and 2 (B). Blue and gray lines indicate dielectric constant of water-ice and basalt, respectively. Depth of observed stratigraphy on HiRISE images is shown as black solid lines, and its ± 5 m error-margin is shown as gray rectangles. (C,D) Dielectric constant calculation based on *Ishiyama et al.* (2019). (C) The concept for bulk dielectric constant for a mixture of rock, air, and water-ice. (D) Ternary contour diagram of the bulk dielectric constant following the projection scheme of *Bramson et al.* (2015). A gray triangle zone indicates implausible porosities. Dotted triangle shows pore-filling ice condition.

.wustl.edu/missions/mro/sharad.htm. We analyzed 373 SHARAD radargrams and identified subsurface reflectors (Fig.2).

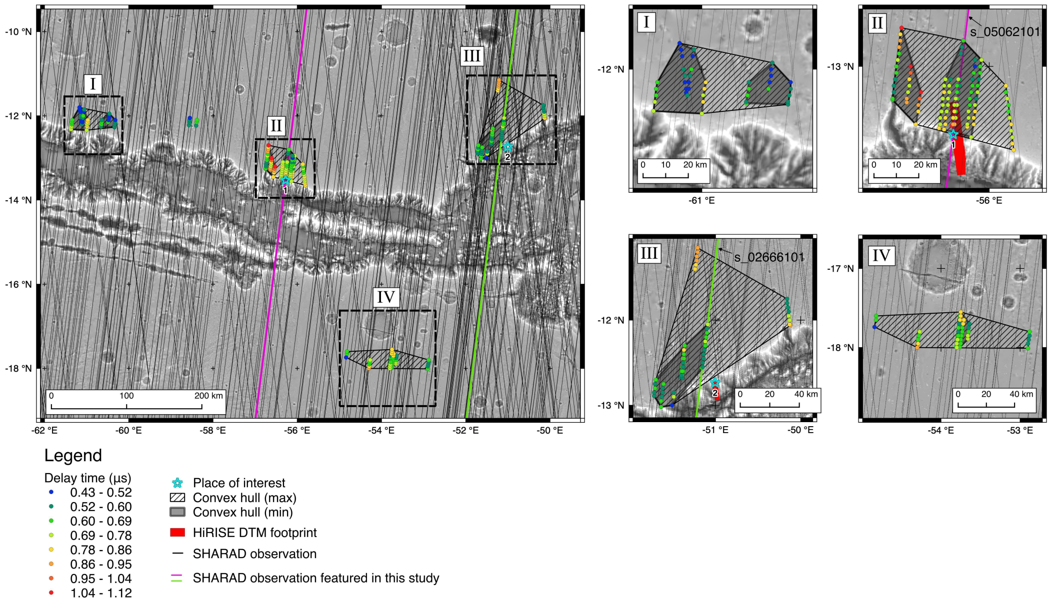

Figure 2. Investigated SHARAD observations (black, magenta, and green lines) and delay time of subsurface echoes (colored filled circles) in eastern Coprates and Capri Chasmata. Locations of the small maps on the right are shown in the larger left map (boxes with dashed outlines). Convex hulls of subsurface echo-identified points correlate to the calculation of coverage in Table 1. The base topographic map was created using HRSC MOLA Blended DEM (*Fergason et al.*, 2018).

We should note that intense nadir and off-nadir surface echoes with their sidelobes could overlap with weak subsurface echoes in the radargrams. Therefore, we performed radar echo simulation by Kirchhoff Approximation Method, which calculates scattered electromagnetic fields at the Martian surface based on Mars Orbiter Laser Altimeter (MOLA) data (Fig.S1B) and obtained simulated radargrams, including surface echoes only. By comparing the observed and simulated radargrams, we can identify subsurface echoes which are only found in observed radargrams. Detailed information for this simulation is shown in the supplementary information. In addition, we checked if the levels of the identified subsurface echoes are more than 10 dB higher than the sidelobe level of the nadir surface echoes. The sidelobe level was estimated based on the Hann window, which is applied in the generation of SHARAD data used in this study. Considering this calculation, subsurface reflectance was identified when the observed echo signal was 10 dB+ larger than the calculated sidelobe (Fig.3D).

Ishiyama et al. (2019) gives the dielectric constant of a mixture of rocks, vacuum (air) and water-ice as

$$\varepsilon_{bulk} = \varepsilon_{vacuum} + \frac{3b}{1-b}\varepsilon_{vacuum} \tag{1}$$

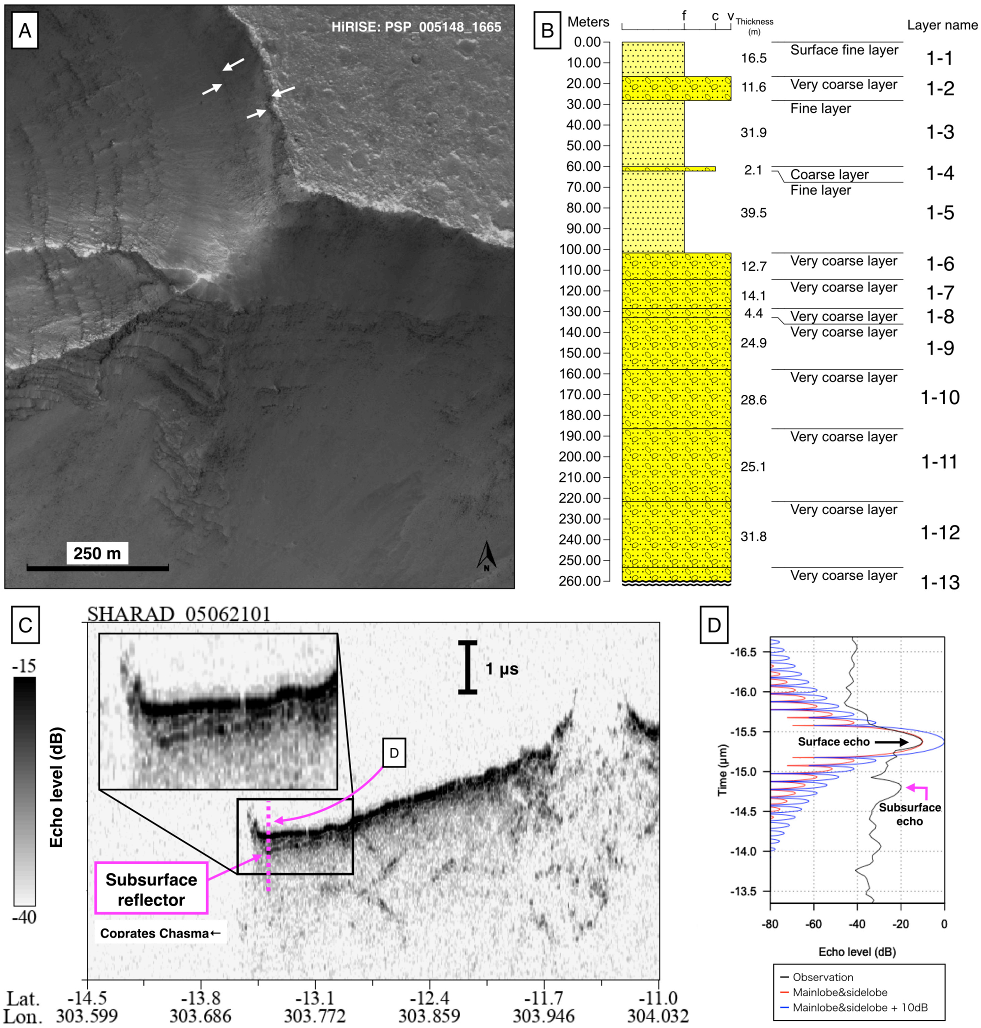

Figure 3. (A) Exposed stratigraphy on the wall, (B) its identified stratigraphy, and (C) its corresponding radargram at Point 1 in Fig.2. The thickness of each layer on the stratigraphic column (B) was measured on a HiRISE DTM (DTEED_014114_1665_005148_1665_A01.IMG). (D) The echo level versus delay time (black line). Red and blue lines indicate sidelobe and sidelobe+10 dB.

$$b = \phi_{ice}\frac{\varepsilon_{ice} - \varepsilon_{vacuum}}{\varepsilon_{ice} + 2\varepsilon_{vacuum}} + \phi_{rock}\frac{\varepsilon_{rock} - \varepsilon_{vacuum}}{\varepsilon_{rock} + 2\varepsilon_{vacuum}} \tag{2}$$

where ε_{vacuum}, ε_{rock}, ε_{ice} are the dielectric constants of vacuum, rock and water-ice (Fig.1C). Volume fractions of rock and ice in a target layer are shown as ϕ_{rock} and ϕ_{ice}. In the calculation, we applied $\varepsilon_{vacuum} = 1$ and $\varepsilon_{ice} = 3.15$ (pure water-ice; *Matsuoka et al.* (1997)). Several previous studies applied a rock dielectric constant around 8 (e.g., *Bramson et al.*, 2015) though such low dielectric constants are measured in non-porous dacite (e.g., 7.54 for Mount Meager - Ring Creek dacite samples, *Rust et al.* (1999)). In this study, we applied $\varepsilon_{rock} = 14.9$ (an average of 14.768 and 14.955 for Mauna Ulu basaltic lava basalt with no voids; *Rust et al.* (1999)), since most of the observed rock on Mars has low-SiO_2 components, which are comparable to basalt and andesite (*McSween et al.*, 2009). Using these equations and parameters, we estimated the plausible component materials in layers above identified subsurface reflectors (Fig.1D).

From SHARAD observation data, we obtained the two-way delay time (Δt) of subsurface reflectors and calculated their depths (d) by assigning a range of dielectric constants (ε: 2 to 16) as

$$d = \frac{\Delta t \times c}{2} \times \frac{1}{\sqrt{\varepsilon_{bulk}}} \tag{3}$$

where c is the speed of light in a vacuum (3.0×10^8 m/s).

3 Results

We identified subsurface reflectors in four areas (I, II, III, and IV) of eastern Coprates and northern Capri Chasmata (Fig.2). Areas I, II, and III are located at the edge of the chasma plateau. Areas II and III are close to tiny tributary chasmata (Figs.2,S2). Area IV is located south of the Saravan crater. Though there are many RSLs that have been found in eastern Coprates and Capri Chasmata (*Chojnacki et al.*, 2016; *Stillman et al.*, 2017), their distribution pattern is not correlated with the subsurface reflector identified in this study. In this region, RSLs are located on Nectaris Montes inside the chasmata; a difficult place to see subsurface on SHARAD data due to its relatively small area and rough surface. The coverage of the four areas as concave hulls of subsurface reflector-identified places is 0.3 – 1.1 $\times10^4$ km^2 in total and Table 1 shows the value for each one. The average delay times of the subsurface echoes for these four areas is 0.67 μs and those for each area are shown in Table 1.

At point 1 in area II, we identified several stratigraphic layers (Fig.3A,B). The uppermost fine layer (1-1) is 16.5 m thick, and the very coarse layer (1-2) has 11.6 m thickness. Beneath these layers, a 31.9 m thick fine layer (1-3) and a 2.1 m thick very coarse subsurface layer (1-4) exist. Layer 1-4 corresponds to the strong layer described by *Beyer and McEwen* (2005). As noted in Bramson et al., 2015, shallow reflectors within $\sim$ 30 m depth from the surface are obscured by sidelobes. Therefore we regarded the delays of the subsurface echoes (0.73 μs in average of area II) as representing bulk information of the dielectric constant above the reflectors (i.e., layers 1-1, 1-2, and 1-3). At point 1, the plausible bulk dielectric constant of the layers above the subsurface reflectors (delay time of the echoes from them: 0.73 μs), which corresponds to the boundaries between the fine and coarse layers at a depth of 60.0 m (bottom of layer 1-3 = top of layer 1-4), is estimated to be 3.4 (Fig.1A). Regarding the error of reading for depth/thickness on a DTM as $\pm$5 m, the range of plausible bulk dielectric constant is 2.6 to 4.2. Since the other remote sensing data

Table 1. Average two-way delay time of the subsurface echoes and coverage of the subsurface reflectors in each area. Area name corresponds to Fig.2. The coverage was calculated as a convex hull of the identified points in Fig.2.

Area name	Average delay time (μs)	Area (km^2)[1]
I	0.58	782.5 – 1411.8
II	0.73	846.4 – 1998.5
III	0.66	925.1 – 5259.0
IV	0.67	153.2 – 2251.5
Total		2707.2 – 10920.7

[1] Minimum: only for main clusters of subsurface echo-identified points in shadow convex hulls of Fig.2. Maximum: for whole subsurface echo-identified points in hatched convex hulls of Fig.2

such as HiRISE color images and CRISM absorptions does not show strong features for water-ice on the chasma wall, layers 1-1, 1-2, and 1-3 are believed to be a pore-filling ice regime, not an excess ice regime (*Bramson et al.*, 2015). Assuming that these layers are pore-filling ice regime, the value of the calculated dielectric constant ($\sim$ 3.4) is consistent with a rock-air mixture with 46.1 % porosity and a rock-air-ice mixture, for which the range of volume fraction of water-ice is 0 – 7.8 % (Fig.1D).

At point 2 in area III, the uppermost fine layer (2-1) has 7.8 m thickness, and the very coarse subsurface layer (2-2) has 6.6 m thickness (Fig.S2). Beneath these layers, a 32.6 m thick fine layer (2-3) and 20.0 m thick very coarse layer (2-4) exist. Layer 2-4 corresponds to the strong layer described by *Beyer and McEwen* (2005). The bulk dielectric constant of the layers above the subsurface reflectors (average delay time in area III: 0.66 μs), which corresponds to the boundary between the fine and coarse layers at a depth of 46.9 m (bottom of layer 2-3 = top of layer 2-4), is estimated to be 4.0 (range of 3.3 to 5.1, considering the error of depth/thickness reading)(Fig.1B). This value is consistent with 39.3 % porosity for the rock-air mixture and up to 21.2 % of the volume fraction of ice for the rock-air-ice mixture (Fig.1D).

4 Discussion and conclusion

From the analysis of radar sounding data, high-resolution images and topographic data, we found that eastern Coprates and Capri Chasmata have areas with relatively low dielectric constants. The calculated bulk dielectric constant (3.4–4.0) suggests that the layers are composed of a rock-air mixture with up to $\sim$ 46.1 % porosity and a rock-ice-air mixture with up to $\sim$ 21.2 % volume fraction of water-ice. In the equatorial region, it has been estimated that water-ice is unstable due to the sublimation and thus a cryosphere does not currently exist (*Schorghofer and Aharonson*, 2005). Considering the instability of ice, the layers with low bulk dielectric constant should be a porous rock layer without water-ice. It is certainly true that $\sim$ 46 % of the calculated porosity in this study is possible for general geologic materials such as those of aeolian, fluvial, and volcanic origins (*Todd and Mays*, 2005), which possibly exist in eastern Coprates and Capri Chasmata. However, orbital simulations have suggested that the obliquity of Mars oscillates periodically. In this case, water could be transported to the low-latitude region at the high obliquity stage. *Head et al.* (2003) evaluates that the last high obliquity stage occurred $\sim$ 0.4 Myr ago. *Bryson et al.* (2008) performed the experiments on the sublimation rate of water-ice beneath regolith, and their conclusion suggests that $\sim$ 1 m-thick water-ice can be maintained for 0.4 Myr under $\sim$ 2 m-thick regolith. Although the age of the low dielectric constant layer is uncertain, if ice was deposited in the layer $\sim$ 0.4 Myr ago, the existence of water-ice at the depth in which the reflector was identified ($\sim$ 60 m) cannot be ruled out. From crater counting, the age of water-ice detected by radar sounding in the mid-latitude area is evaluated to be $\sim$ 20 Myr (*Viola et al.*, 2015). Thus, if the layers in the equatorial area contain water-ice, the time when water-ice was deposited should differ between mid-latitude and low-latitude regions. In addition to the preservation of water-ice at a time of high-obliquity, the accumulation of water-ice in the pores by thermal contraction is also suggested (*Fisher*, 2005), which may be the another origin of pore water-ice in eastern Coprates and Capri Chasmata.

If the layer is composed of a rock-ice-air mixture, using the estimated water-ice volume fraction in a layer of a specific thickness, the possible amount of water-ice can be calculated. In area II, assuming a layer 846.4 to 1998.5 km^2 that is 60.0 m thick with 7.8 % volume fraction of water-ice, 4.0 to 9.4 km^3 of putative water-ice would exist. However, considering the emplacement of water-ice in 0.4 Ma by snowfall (e.g., *Christensen*, 2003), it is natural to think a host layer of water-ice is located above the strong layer, which is described as a Hesperian lava flow (*Witbeck et al.*, 1991). This stratigraphic setting (water-ice can exist in the topmost layer) leads to the volume fraction of putative water-ice in the topmost layer being 29 %. This calculation can be applied to 925 to 5258 km^2 of the subsurface reflectors region in area III. Based on the analysis of radar sounding data, in point 2 in area III, the plausible water-ice volume fraction of a 46.9 m thick layer is 21.2 %. Although this condition simply leads to a volume range of putative water-ice from 9.2 to 52.4 km^3, the volume of putative water-ice in area III would be less than 7.2 km^3 assuming a pore-filling water-ice regime (less than 50 % water-ice content) in the 5259.0 km^2-extent of a 7.8 m-thick topmost layer. Therefore, a maximum of 16.6 km^3 of putative water-ice may exist in the plateau of eastern Coprates and northern Capri Chasmata. On the gamma-ray spectrum, eastern Coprates and Capri Chasmata do not show a strong hydrogen concentration (*Boynton et al.*, 2007). Since the detection depth of the hydrogen is approximately 1 m (*Feldman et al.*, 2004), the water-ice layers in these regions are thought to be undetectable by the gamma-ray spectrum. The surface echo power analyses of radar sounding data by the Mars Advanced Radar for Subsurface and Ionospheric Sounding instrument (MARSIS) showed the dielectric constant property at a few decameters below the surface (*Mouginot et al.*, 2010). On their dielectric map, dielectric constants in eastern Coprates and Capri Chasmata decrease from southwest to northeast. This suggests drastic variation in the shallow subsurface environment, such as from dry to ice-rich or the increase of porosity in these areas. Thus, although deducing accumulation mechanisms is still challenging, our analyses imply the possible existence of a subsurface ice-contained layer in eastern Coprates and northern Capri Chasmata, i.e., even in the equatorial region.

In this work, from the bulk dielectric constant evaluated from the delay time of radar sounding and plausible corresponding depth at the stratigraphic exposure, we could only constrain the upper limit of the water-ice fraction. Thus, considering the current instability of water-ice in low-latitude terrain, further studies and discussions are required to determine the existence of water-ice and, if water-ice actually exists, for the mechanism to maintain it within low-latitude terrain.

Acknowledgments
We used the data of SHARAD and HiRISE on the Planetary Data System and the website of the University of Arizona (`https://hirise.lpl.arizona.edu/`). HiRISE DTMs have been processed with the MarsSI (`https://marssi.univ-lyon1.fr/`

MarsSI/) application with the support of Matthieu Volat. Discussion with Isaac B Smith greatly improved our analysis. We appreciate Lucy Kwok for the generous effort of editing the English in this manuscript. We also thank J. L. Whitten and an anonymous reviewer for their thorough reviews. This work was supported by the JSPS Grants-in-Aid for Scientific Research (KAKENHI 17H06459 and 19H00707).

References

Beyer, R.A. and A.S. McEwen, 2005, Layering stratigraphy of eastern Coprates and northern Capri Chasmata, Mars, *Icarus*, *179*(1), 1–23.

Boynton, W.V., et al., 2007, Concentration of H, Si, Cl, K, Fe, and Th in the low- and mid- latitude regions of Mars, *J. Geophys. Res.*, **112** E12.

Bramson, A.M., S. Byrne, N.E. Putzig, S. Sutton, J.J. Plaut, T.C. Brothers, and J.W. Holt, 2015, Widespread excess ice in Arcadia Planitia, Mars, *Geophys. Res. Lett.,* **42**(16), 6566–6574.

Bryson, K.L., V. Chevrier, D.W. Sears, and R. Ulrich, 2008, Stability of ice on Mars and the water vapor diurnal cycle: Experimental study of the sublimation of ice through a fine-grained basaltic regolith, *Icarus*, *196*(2), 446–458.

Byrne, S., C.N. Dundas, M.R. Kennedy, M.T. Mellon, A.S. McEwen, S.C. Cull et al., 2009, Distribution of mid-latitude ground ice on Mars from new impact craters, *Science*, 325.5948: 1674–1676.

Carr, M.H., and J.W. Head, 2010, Geologic history of Mars, *Earth and Planet. Sci. Lett.*, **294**, 185–203, doi:10.1016/j.epsl.2009.06.042.

Chojnacki, M., and B.M. Hynek, 2008, Geological context of water- altered minerals in Valles Marineris, Mars, *J. Geophys. Res.*, **113** E12.

Chojnacki, M., A. McEwen, C. Dundas, L. Ojha, A. Urso, and S. Sutton, 2016, Geologic context of recurring slope lineae in Melas and Coprates Chasmata, Mars, *J. Geophys. Res.*, **121**(7), 1204–1231.

Christensen, P.R., 2003, Formation of recent Martian gullies through melting of extensive water-rich snow deposits, *Nature*, 422(6927), 45.

Clifford, S.M., J. Lasue, E. Heggy, J. Boisson, P. McGovern, and M.D. Max, 2010, Depth of the Martian cryosphere: Revised estimates and implications for the existence and detection of subpermafrost groundwater, *J. Geophys. Res.*, **115**, E7.

Dundas, C.M., S. Byrne, A.S. McEwen, M.T. Mellon, M.R. Kennedy, I.J. Daubar, and L. Saper, 2014, HiRISE observations of new impact craters exposing Martian ground ice, *J. Geophys. Res.*, **119**(1), 109–127.

Dundas, C.M., A.S. McEwen, M. Chojnacki et al., 2017, Granular flows at recurring slope lineae on Mars indicate a limited role for liquid water, *Nature Geosci.*, **10**, 903–907, doi:10.1038/s41561-017-0012-5.

Dundas, C.M. et al., 2018, Exposed subsurface ice sheets in the Martian mid-latitudes, *Science*, 359.6372: 199–201.

Feldman, W.C. et al., 2004, Global distribution of near- surface hydrogen on Mars, *J. Geophys. Res.*, **109**(E9).

Fergason, R.L, Hare, T.M., Laura, J., 2018, HRSC and MOLA Blended Digital Elevation Model at 200m v2, Astrogeology PDS Annex, U.S. Geological Survey, URL: `http://bit.ly/HRSC_MOLA_Blend_v0`

Fisher, D.A., 2005, A process to make massive ice in the martian regolith using long-term diffusion and thermal cracking, *Icarus*, **179**(2), 387–397.

Head, J.W. and D.R. Marchant, 2003, Cold-based mountain glaciers on Mars: western Arsia Mons, *Geology*, 31(7), 641–644.

Head, J.W., J.F. Mustard, M.A. Kreslavsky, R.E. Milliken, and D.R. Marchant, 2003, Recent ice ages on Mars, *Nature*, 426(6968), 797.

Ishiyama, K., A. Kumamoto, Y. Takagi, N. Nakamura, and S. Hasegawa, 2019, Effect of crack direction around laboratory-scale craters on material bulk permittivity, *Icarus*, **319**, 512–524.

Matsuoka, T., S. Fujita, and S. Mae, 1997, Dielectric properties of ice containing ionic impurities at microwave frequencies, *J. Phys. Chem. B*, **101**(32), 6219–6222.

McSween, H.Y., G.J. Taylor, and M.B. Wyatt, 2009, Elemental composition of the Martian crust, *Science*, **324**(5928), 736–739.

Milkovich, S.M., J.W. Head, and D.R. Marchant, 2006, Debris-covered piedmont glaciers along the northwest flank of the Olympus Mons scarp: Evidence for low-latitude ice accumulation during the Late Amazonian of Mars, *Icarus*, **181**(2), 388–407.

Mellon, M. T., et al., 2009, Ground ice at the Phoenix Landing Site: Stability state and origin, *J. Geophys. Res.*, **114**, E00E07, doi:10.1029/2009JE003417.

Morgan, G.A. et al., 2019, The Mars Subsurface water-ice Mapping (SWIM) Project, paper presented at the 50th Lunar and Planetary Science Conference, Lunar and Planetary Institute, The Woodlands, Tex.

Mouginot, J. et al., 2010, The 3–5 MHz global reflectivity map of Mars by MARSIS/Mars Express: Implications for the current inventory of subsurface H_2O, *Icarus*, **210**(2), 612–625.

Orosei, R. et al., 2018, Radar evidence of subglacial liquid water on Mars, *Science*, **361**(6401), 490–493.

Putzig, N.E., I.B. Smith, M.R. Perry, F.J. Foss II, B.A. Campbell, R.J. Phillips, and R. Seu, 2018, Three-dimensional radar imaging of structures and craters in the Martian polar caps, *Icarus*, **308**, 138–147.

Quantin-Nataf, C. et al., 2018, MarsSI: Martian surface data processing information system, *Planetary and Space Science*, **150**, 157–170.

Rust, A.C., J.K. Russell, and R.J. Knight, 1999, Dielectric constant as a predictor of porosity in dry volcanic rocks, *J. Volcanol. Geotherm. Res.*, **91**(1), 79–96.

Seu, R. et al., 2004, SHARAD: The MRO 2005 shallow radar, *Planetary and Space Science*, **52**(1-3), 157–166.

Smith, I.B., C. Viviano, M. Chojnacki, N.E. Putzig, C. Quantin, and J.A.P. Rodriguez, 2019, Characterization of Hydrated, Layered Deposits at Valles Marineris Plateau, a Multidisciplinary Approach, paper presented at the 50th Lunar and Planetary Science Conference, Lunar and Planetary Institute, The Woodlands, Tex.

Stillman, D.E., T.I. Michaels, and R.E. Grimm, 2017, Characteristics of the numerous and widespread recurring slope lineae (RSL) in Valles Marineris, Mars, *Icarus*, **285**, 195–210.

Schorghofer, N., and O. Aharonson, 2005, Stability and exchange of subsurface ice on Mars, *J. Geophys. Res.*, **110**, E5.

Stuurman, C.M., G.R. Osinski, J.W. Holt, J.S. Levy, T.C. Brothers, M. Kerrigan, and B.A. Campbell, 2016, SHARAD detection and characterization of subsurface water ice deposits in Utopia Planitia, Mars, *Geophys. Res. Lett.*, **43**, 9484–9491, doi:10.1002/2016GL070138.

Todd, D.K. and L.W. Mays, 2005, Groundwater hydrology, 3rd ed, pp 636.

Touma, J., and J. Wisdom, 1993, The chaotic obliquity of Mars, *Science*, **259**(5099), 1294–1297.

Viola, D., A.S. McEwen, C.M. Dundas, and S. Byrne, 2015, Expanded secondary craters in the Arcadia Planitia region, Mars: Evidence for tens of Myr-old shallow subsurface ice. Icarus, *Icarus*, **248**, 190–204.

Witbeck, N.E., K.L. Tanaka, and D.H. Scott, 1991, Geologic map of the Valles Marineris region, Mars, No. MAP I-2010, US Geological Survey Report.

Supporting Information for "Radar sounding of subsurface water-ice in eastern Coprates and Capri Chasmata, Mars"

R. Noguchi[1], K. Ishiyama[1,2], A. Kumamoto[3], C. Uemura[4], Y. Kasaba[3], T. Usui[1,5], A. Oura[3], and D. Shoji[5]

[1]Institute of Space and Astronautical Science, Japan Astronautical Exploration Agency, 3-1-1 Yoshinodai, 252-5210, Sagamihara, Kanagawa, Japan

[2]National Institute of Technology, Tsuruoka College, 104 Sawada, Inooka, Tsuruoka, Yamagata 997-8511, Japan

[3]Tohoku University, Aramaki-Aza-Aoba 6-3, Aoba-ku, Sendai, Miyagi, 980-8578, Japan

[4]SOKENDAI (Graduate University for Advanced Studies), 3-1-1 Yoshinodai, Sagamihara, Kanagawa, 252-5210, Japan

[5]Earth-Life Science Institute, Tokyo Institute of Technology, 2-12-1 Ookayama, Meguro, Tokyo, 152-8550, Japan

Contents of this file

1. Text S1. Kirchhoff approximation method for the clutter simulation
2. Text S2. Component calculation in the case of the dielectric constant of non-porous rock being 8

Additional Supporting Information (Files uploaded separately)

---

1. Figure S1. An example of (A and B: original, C and D: interpreted reflectances are marked) SHARAD radargrams and (E,F) surface clutter-simulated radargrams. The simulation method is shown in the supplementary information.

2. Figure S2. (A) Exposed stratigraphy on the wall, (B) its identified stratigraphy, and (C) its corresponding radargram at Point 2 in Fig.1. The thickness of each layer on the stratigraphic column (B) was measured on a HiRISE DTM (HI_038733_1670_042478_1670-ALIGN-DEM.tiff). (D) The echo level versus delay time (black line). Red and blue lines indicate sidelobe and sidelobe +10 dB.

3. Figure S3. Topography map of Coprates Chasma. Base of the upper map was created using HRSC MOLA Blended DEM (Fergason et al., 2018). Hatched boxes indicate tiny nameless valleys (A, B, and C). CTX mosaic of each valley is shown in lower maps.

4. Data S1. SHARAD observation list which was used in this study.

5. Data S2. Locations of identified SHARAD reflectors.

6. Data S3. HiRISE DTM used in this study.

Kirchhoff approximation method for the clutter simulation

The simulated radargrams were created using Mars digital elevation model (DEM) and spacecraft locations during SHARAD operation. Mars DEM was based on the MOLA Mission Experiment Gridded Data Records (https://pds-geosciences.wustl.edu/mgs/mgs-m-mola-5-megdr-l3-v1/mgsl_300x/meg128/). Their resolution was 128 pixel per degree. Spacecraft locations were from geometry table files in PDS data provided by the U.S. SHARAD team (https://pds-geosciences.wustl.edu/mro/mro-m-sharad-5-radargram-v1/mrosh_2001/data/geom/). Assuming Kirchhoff approximation, the electromagnetic field scattered from a rough surface can be calculated as the summation of the electromagnetic field scattered from local micro planes. Using Mars DEM, the Mars surface within 3 degrees of latitude and longitude from the spacecraft nadir point (S) were divided into micro square planes with horizontal size of 1/1280 degree of longitude and latitude (dS). Then we calculated the direction from spacecraft to micro plane eR, normal direction of micro plane n, distance from the spacecraft to micro plane R, incident magnetic field at micro plane H_i, and derived the scattered electric field E_s using the Franz formula for perfect electric conductor (PEC) plane

$$E_s = 2ikZ_0 \int_S e_R \times \{e_R \times (n \times H_i)\} \frac{\exp(ikR)}{4\pi R} dS \tag{1}$$

where k is wave number of the electromagnetic wave, and Z_0 is wave impedance (120π). In the above calculation, we only assumed a PEC rough surface without any subsurface reflectors for reduction of calculation. So, we should note that simulated radargrams only include surface echoes whose intensity is different from observation due to reflectance difference from the actual one. On the other hand, the surface echo patterns (distance to the reflection point on the surface, R) found in the simulated radargram are expected to be the same as those in the observed radargram.

Component calculation in the case of the dielectric constant of non-porous rock being 8

In converting dielectric constants to composition, we assumed the rock portion was non-porous basalt. In the main text, we applied a value which is shown as non-porous basalt (14.9, an average of 14.768 and 14.955 for Mauna Ulu basaltic lava, Rust et al., 1999) since most of the observed rock on Mars has low-SiO_2 components which are comparable to basalt and andesite McSween et al., 2009. However, several previous studies applied a lower rock dielectric constant (e.g., 8 is applied in Bramson et al., 2015). Here we show the results of a component calculation in the case of the dielectric constant of non-porous rock being 8 to help to compare with other studies/fields.

At point 1 in area II, assuming that these layers are pore-filling ice regime, the value of the calculated dielectric constant ($\sim$3.4) is consistent with a rock-air mixture with 36.6 % porosity (possible value in general geologic materials, Todd and Mays2005) and a rock-air-ice mixture, for which the range of volume fraction of water-ice is 0 – 21.4 % (Fig.A1). This simply leads to a maximum of 25.7 km^3 of putative water-ice, though such a large volume of water-ice is not possible considering the stratigraphic setting (water-ice can exist in the topmost layer considering the possible emplacement of snow at 0.4 Ma) as shown in the discussion in the main text.

At point 2 in area III, assuming that these layers are pore-filling ice regime, the value of the calculated dielectric constant ($\sim$4.0) is consistent with a rock-air mixture with 28.8 % porosity (possible value in general geologic materials, Todd and Mays, 2005) and a rock-air-ice mixture, of which the range of the volume fraction of ice is 0 – 34.7 % (Fig.A1). This simply leads to a maximum of 85.8 km^3 of putative water-ice, though such a large volume of water-ice is not possible considering the stratigraphic setting as shown in the discussion in the main text.

Reference

Bramson, A.M., S. Byrne, N.E. Putzig, S. Sutton, J.J. Plaut, T.C. Brothers, and J.W. Holt, 2015, Widespread excess ice in Arcadia Planitia, Mars, *Geophys. Res. Lett.,* **42**(16), 6566–6574.

McSween, H.Y., G.J. Taylor, and M.B. Wyatt, 2009, Elemental composition of the Martian crust, *Science*, **324**(5928), 736–739.

Rust, A.C., J.K. Russell, and R.J. Knight, 1999, Dielectric constant as a predictor of porosity in dry volcanic rocks, *J. Volcanol. Geotherm. Res.*, **91**(1), 79–96.

Todd, D.K. and L.W. Mays, 2005, Groundwater hydrology, 3rd ed, pp 636.

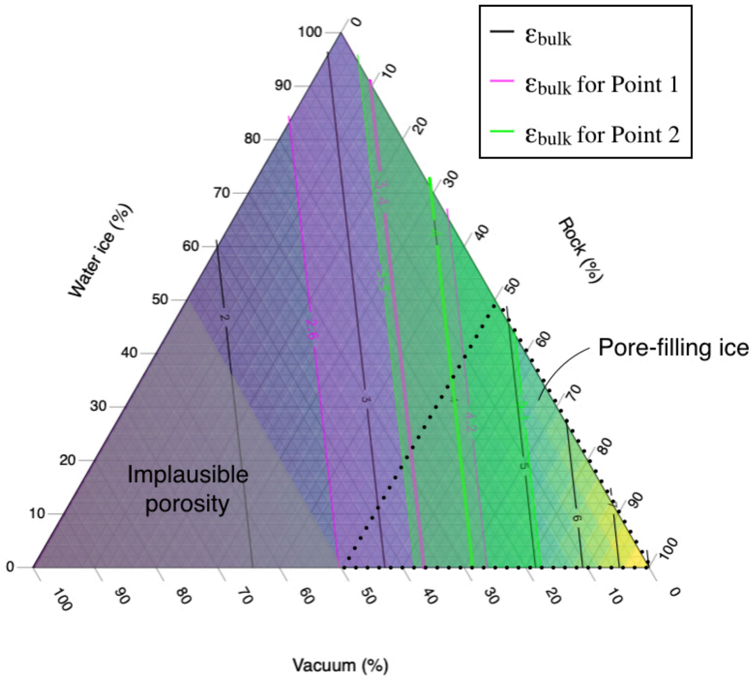

Figure A1. Ternary contour diagram of the bulk dielectric constant following the projection scheme of Bramson et al., 2015 using a dielectric constant of non-porous rock as 8. A gray triangle zone indicates implausible porosities. Dotted triangle shows pore-filling ice conditions.